A Dynamical Framework that Integrates Optical and SAR Imagery for Sugarcane Monitoring in the Cauca Valley

Alejandro Mestre-Quereda, *Member, IEEE*, Tomas Martinez-Marin *Member, IEEE*, Juan M. Lopez-Sanchez, *Senior Member, IEEE*, Carlos Mosquera, Henk Pelgrum, Antonia Skarli, Dirk Hoekman, and Corné van der Sande.

***Abstract*—In this work, we present a novel dynamical framework for crop monitoring that integrates SAR and optical satellite imagery. The proposed methodology employs two-dimensional state transitions to explicitly model the expected temporal evolution of crops. By combining such crop modeling with multi-sensor observations, including dual-polarimetric (VV and VH) radar images gathered by Sentinel-1 and optical imagery from Sentinel-2, the developed framework produces robust and consistent estimations using the well-established Kalman Filter. Specifically, the approach is applied to retrieve the biomass values of sugarcane crops located in the Cauca Valley (Colombia), over a full growing season (from summer 2024 to summer 2025). An intensive field campaign was carried out, so that ground-truth measurements in a large number of points, located in multiple fields, were available to develop and validate the proposed integration algorithm. Results show that biomass is accurately estimated especially when all available observations, both SAR and optical, are employed. In this case, a global root mean square error of 0.103 kg, a mean absolute error of 0.064 kg and an accumulated biomass difference of 13.8 kg·day are obtained after evaluating the model multiple times on randomly-selected points. The analysis also highlights a key limitation of optical imagery in the study area, as a large number of images are affected by cloud cover, resulting in long gaps within the time series and reduced estimation accuracy. Furthermore, the best performance of the proposed integrated model is achieved when all available SAR products, including dual-polarization (VV and VH) coherence and intensity products, are exploited, although very good results are also obtained using single-polarization coherence and intensity data (either at VV or VH polarizations). Comparison with alternative approaches, including partially integrated methods using only one type of information (either SAR or NDVI), and methods based solely on machine learning, indicates that the proposed methodology consistently offers superior accuracy in biomass estimation.**

***Index Terms*—Agriculture, Dynamic Systems Theory, Phenology, Kalman Filtering, Remote Sensing, Synthetic Aperture Radar, NDVI**

I. Introduction

REMOTE sensing and satellite imagery have become essential tools for agricultural monitoring. Their adoption has increased substantially due to their cost-effectiveness and scalability in assessing crop conditions, estimating yields, and facilitating sustainable land management [1], [2], [3], [4], [5], [6], [7], [8]. These technological advancements are particularly critical in addressing the challenges posed by climate variability, enhancing resource-use efficiency, and meeting the growing demand for timely and accurate agricultural data.

Traditionally, optical sensors have been widely used for agricultural applications because of their high sensitivity to vegetation characteristics. By capturing the way plants reflect and absorb different wavelengths of light, these sensors can detect subtle changes in crop health, nutrient status, and stress conditions [9].

However, the major limitation of optical imagery is its dependence on cloud-free conditions. The presence of clouds prevents the sensor from capturing the status of Earth's surface, resulting in images that lack useful information for agricultural monitoring. More importantly, persistent cloud presence leads to substantial gaps in the temporal series of optical data, disrupting the continuity essential for accurate time-series analysis [10]. Accordingly, the implementation of reliable monitoring tools may be affected, as the absence of consistent observations constrains the accurate tracking of crop dynamics and limits the capacity to generate timely and comprehensive agricultural assessments.

In this context, the use of synthetic aperture radar (SAR) imagery [11], [12], which can be acquired independently of weather conditions and solar illumination, has progressively gained attention as an alternative technology for agricultural applications [13], [14]. Many different methodologies based on SAR data have been proposed to monitor crop growth. For instance, some approaches directly exploit radar features using decision trees, Wishart classifiers, or Machine Learning methods, to estimate the phenological states of crops [15], [16], [17], [18]. Alternatively, other works adopt a *dynamical* approach [19], [20], [21], [22], [23], [24], [25]. In this framework, Bayesian Filtering (BF) techniques, like Extended Kalman Filtering (EKF) and Particle Filtering (PF), are employed to combine crop growth dynamics with SAR observations, thereby providing estimates of the crop phenology or other biophysical variables in an integrated way. This dynamic methodology was first demonstrated in [20] for rice monitoring using TerraSAR-X data. A related EKF-based strategy was later presented in [21], applying C-band RADARSAT-2 imagery to retrieve the phenology of other cereal crops. The PF was subsequently introduced in [22], [19] to estimate both phenological stages and key agricultural dates (e.g., sowing and panicle initiation) in rice fields. Furthermore, a data fusion

A. Mestre-Quereda, T. Martinez-Marin and J. M. Lopez-Sanchez are with the Institute for Computer Research (IUII), University of Alicante, P.O.Box 99, E-03080 Alicante, Spain (e-mail: alejandro.mestre@ua.es, tomas.martinez@ua.es, juanma-lopez@ieee.org).

C. Mosquera is with AgroAp, C.I. AGROAP SAS, Ka 100 #11-60, ofi. 819. Cali, Valle, Colombia (e-mail: carlosmosquera@agroap.com).

H. Pelgrum, A. Skarli amd C. van der Sande are with eLEAF, Stadsring 65B, 3811 HN Amersfoort, The Netherlands (e-mail: Henk.Pelgrum@eleaf.com, antonia.skarli@eleaf.com, corne.van.der.sande@eleaf.com).

D. Hoekman is with SarVision, Agro Business Park 10, 6708 PW Wageningen, The Netherlands (e-mail: hoekman@sarvision.nl).

approach combining SAR, NDVI, and temperature information was proposed for rice in [23]. The advantages of combining different sources of data are evident. Firstly, both the accuracy and reliability of estimates can be improved, as errors or uncertainties from one dataset can be compensated by another. Secondly, it leverages complementary information, since different sensors capture distinct aspects of crop dynamics. More importantly, fusion also ensures temporal continuity, allowing monitoring to go on even when remote sensing data are unavailable (e.g., optical imagery under cloudy conditions). Finally, it enhances generalization across varying environmental conditions, leading to more robust and consistent monitoring operation.

Regarding the use of Earth observation data for sugarcane monitoring, which was reviewed in [26], there is no successful monitoring approach exploiting radar data for complementing optical satellite for providing continuous estimates of biophysical variables. There are works focused on harvest detection [27] and others on productivity mapping [28]. In addition, an approach based on machine learning for detecting four phenological stages was presented in [29]. Consequently, a methodology for sugarcane monitoring that integrates optical and SAR imagery within a unified analytical framework has not been developed yet. In this work, we propose a method based on a dynamical approach which employs the well-known Kalman Filter [30] to derive optimal state estimates. In particular, it is designed to continuously estimate biomass values of the plants throughout the growing season, thereby providing reliable frequent information about crop development. This methodology is implemented and evaluated in the context of sugarcane cultivation in the Cauca Valley, Colombia, which is affected by long cloudy and rainy periods which make only 20% of Sentinel-2 images valid for use. This work was conducted as part of the scientific project 'DINOSAR: Diagnostic Tool that INtegrates Optical, Infrared and SAR data', funded by the European Union Agency for the Space Programme (EUSPA).

The article is structured as follows. Section II describes the reference data and presents a formal description of the proposed integration algorithm. The results obtained and the evaluation of the performance of the proposed method are presented in Section III. A discussion on the contribution and limitations of this method is included in Section IV. Finally, main conclusions are summarized in Section V.

II. Materials and Methods

A. Test Site and Reference Data

The test site is located in the Cauca Valley, Colombia. Sugarcane is a key agricultural crop in this region of the country, mainly because its favourable climate and its long-standing agroindustrial tradition. The valley is the epicentre of the country's sugarcane cultivation, hosting extensive plantations and modern milling facilities that sustain a vertically integrated industry. The conditions in the Cauca Valley allow for year-round cultivation of sugarcane, with no distinct harvest seasons, with approximately 237,000 ha dedicated to its cultivation.

More specifically, the selected study area lies close to the cities of Cali and Palmira, as shown in Fig. 1. It spans an area of approximately 560 km^2 and comprises 34 fields, with a total of 70 measurement points, that are spread over the area and that are selected to conduct the reference data collection campaign. The selected fields include three different environments (soil textures), four different sugarcane varieties, and eight different ratoon ages, and occupy areas between 3.5 ha and 27.6 ha, with an average area of 13.1 ha.

The data collection campaign started in July 2024 and ended in August 2025, so that more than one year of in-situ measurements were collected, covering a complete season for all fields. During the first two months of the season, points were visited weekly. Afterwards, all points were visited every two weeks until the end of the season. For each point of every field, multiple sugarcane variables were manually measured, as summarized in Table I.

TABLE I
Variables measured in the in-situ data collection campaign and their expected dynamic ranges.

Measured Variable	Dynamic Range
Cane height	[0, 400 cm]
Cane diameter (stem)	[0, 5 cm]
Number of Stems per meter ($<$ 3 months)	[0, 56]
Number of Stems per meter ($>$ 3 months)	[0, 16]
Biomass (kg/stem)	[0, 4 kg]
Biomass (kg/leaves)	[0, 0.9 kg]

Figure 2 shows all measurements of total biomass (obtained as the summation of the biomass of stems and leaves) and cane height gathered during the whole season, represented as a function of the date from the beginning of the season of each field (i.e., Day of Season, abbreviated as DoS). For a better illustration of the height and biomass temporal evolution, the measurements are linearly interpolated to obtain daily values. As shown in Figs. 2(a) and (b), both height and biomass are low during the first three months and then increase progressively. Height follows an approximately linear trend over the season, whereas biomass remains very low initially and then rises more quickly. Notably, biomass exhibits considerable fluctuations, with sudden drops and increases observed during the season. In addition, both variables show substantial variability, as some plants grow faster or provide more biomass than others, even within the same field, as a consequence of different cultivation conditions and many external factors. Evidently, this variability must be addressed for accurate modelling.

B. Satellite Images

Satellite images correspond to Sentinel-1 (SAR) and Sentinel-2 (optical) acquired during the whole field campaign, i.e., between July 2024 and August 2025.

Concerning Sentinel-1, all available SLC (Single-Look Complex) images coming from orbit 142 (descending pass) acquired in Interferometric Wide swath (IW) mode were considered. Only images from Sentinel-1A satellite were gathered,

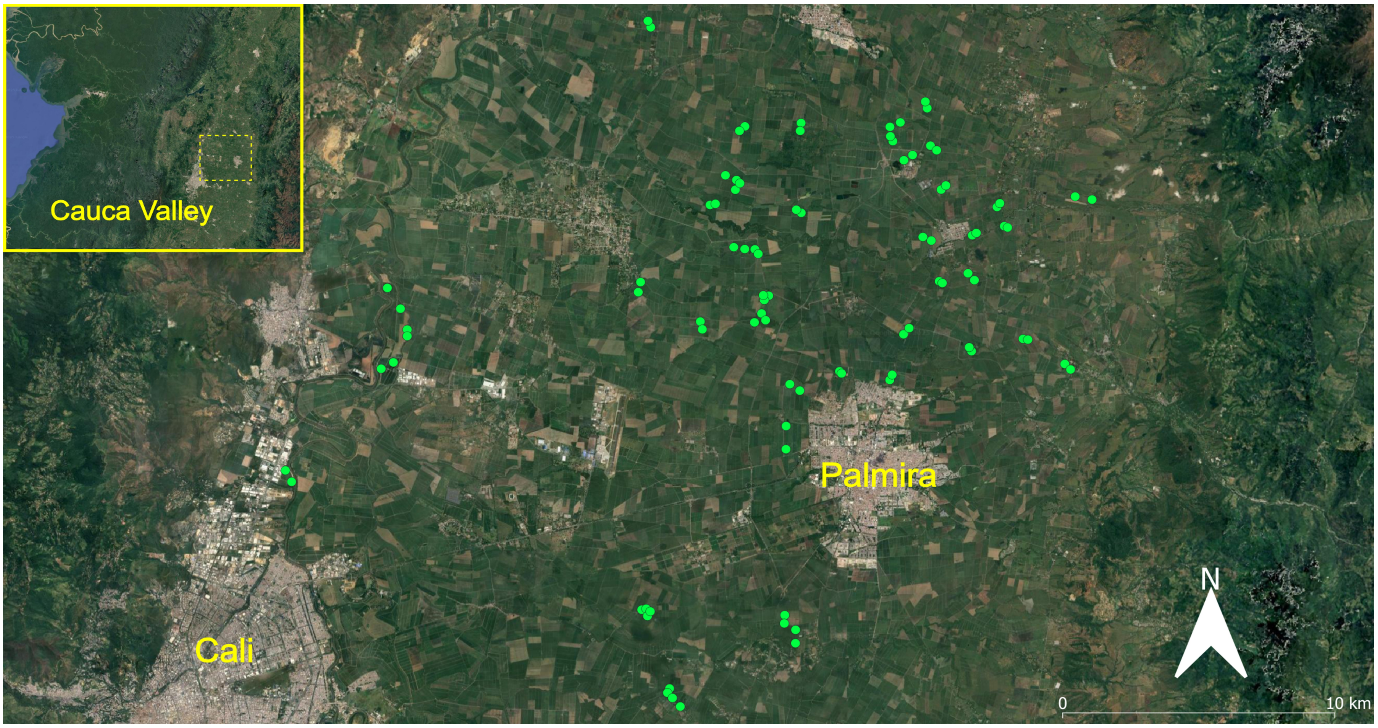

Fig. 1. Optical image of the Cauca Valley with the location of the measurement points (green dots) employed in the in-situ data collection campaign.

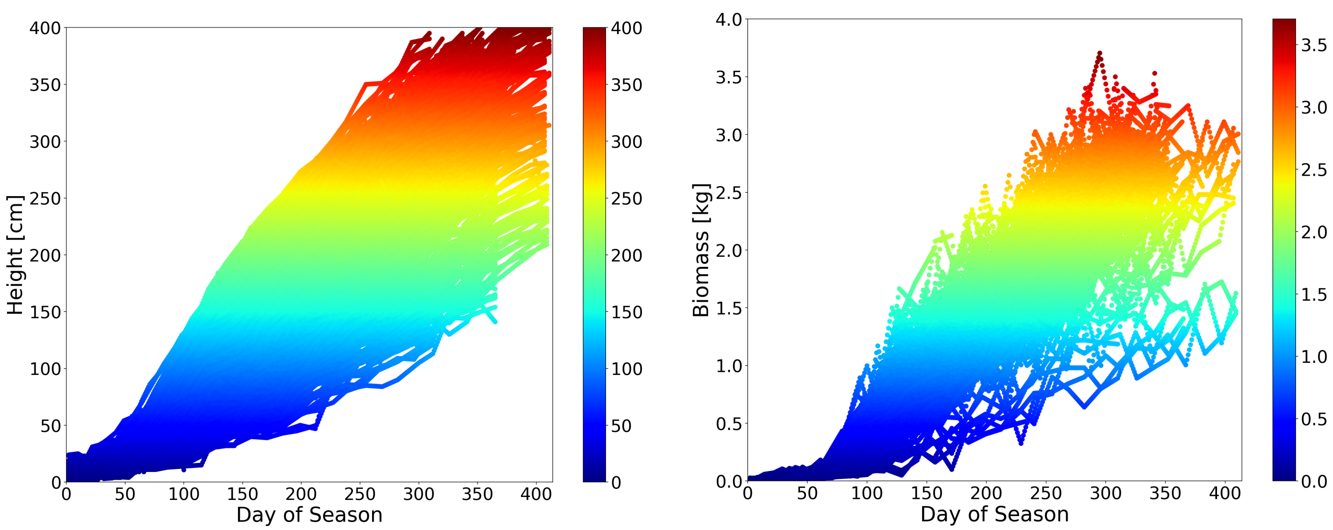

(a) Height measurements.

(b) Biomass measurements.

Fig. 2. Cane height and total biomass measurements for all points selected for the in-situ data campaign.

hence providing a revisit cycle of 12 days. The preprocessing steps carried out with the images were:

1) Coregistration of all images to a common reference image using precise orbital information and the Copernicus DEM (with a spatial resolution of 30 m).
2) Terrain flattening and radiometric calibration to γ_0, in order to generate the backscatter coefficients at both polarizations VV and VH [31].
3) Interferogram generation for all pairs of consecutive dates, both at VV and VH polarimetric channels.
4) Speckle filtering and coherence estimation: a multitemporal filter using 6 consecutive images is used, allowing for a strong speckle removal and a better preservation of edges and features [32], [33], [34], [31]. Also, the filter provides a good compromise between the loss of spatial resolution and the required accuracy in coherence estimation.
5) Geocoding of all intensity (backscatter) and coherence images to a cartographic grid (in latitude/longitude coordinates) with a 10 m posting output.

Regarding optical data, we employed geometrically and atmospherically corrected Level-2 Sentinel-2 products. The NDVI products were computed from the near infrared and red bands. All optical products were resampled to the same geographical grid of the radar products.

C. Integration Algorithm

As previously outlined in Section I, the proposed sugarcane monitoring approach focuses on estimating biomass throughout the growing season, as biomass is the most relevant parameter for monitoring this crop. Compared to other physical variables or vegetation indices, biomass estimates provide more meaningful insights and stronger support for practical decision-making, so that knowing how biomass evolves in time is critical for farmers and other agricultural professionals.

The goal of the integration algorithm is therefore to provide optimal estimates of sugarcane biomass throughout the growing season, by appropriately combining its expected temporal evolution with information derived from satellite observations. This combination of temporal modeling and a set of indirect measurements is very well described in the context of Dynamical Systems Theory [21], [25]. Evidently, in our specific case, we consider sugarcane crops and the biomass they produce as a dynamic system that evolves over time.

The integration algorithm consists of two main components. First, an *evolution model* describes how biomass is expected to change over time. This temporal evolution is described with a state-space model in which the biomass corresponds to the state variable, that is, the key variable that completely represents the dynamic system and that is used to characterize its present and future states and values. Second, an *observation model* establishes the relation between the state variable (biomass) and a set of observations. In our case, the observations are derived from SAR and optical images gathered by the Sentinel-1 and Sentinel-2 satellites, respectively. Since these satellites do not measure biomass directly, the data are treated as indirect measurements of the variable we aim to estimate. The combination of the evolution and observation models is carried out with the well-known Kalman Filter (KF) [30], which provides optimal solutions to many prediction tasks, and constitutes the core of the integration algorithm proposed here.

Since this work focuses on the estimation of a single crop variable (i.e., biomass) throughout a complete season, we follow the formulation of a one-dimensional KF in which the desired variable is treated as a state variable. The filter is composed of two steps: prediction and update. The prediction step provides a prior estimation of the system state by "projecting" its expected evolution ahead by making use of the evolution model. Then, the update step refines the previous estimation by including observations (and therefore by making use of the observation model).

We first introduce the general formulation of the filter to provide the reader with basic information of the process. Then, we will outline which parts are specifically tailored to our specific case.

The first step of the KF corresponds to the prediction, which is done according to:

$$\hat{x}_k = f(\hat{x}_{k-1}), \tag{1}$$

being $\hat{x}_k$ is the predicted state at discrete time k, $\hat{x}_{k-1}$ corresponds to the previous state at time step $k-1$, and f represents the evolution model associated with the temporal evolution of the state variable that is being estimated (usually denoted as temporal model). Note that f in Eq. 1 symbolically describes this temporal evolution of the state variable $\hat{x}$. Specific details on the practical implementation of f are provided in Subsection II-C1.

The estimated uncertainty P_k of the prediction at time k is:

$$P_k = FP_{k-1}F^T + Q_{k-1} \tag{2}$$

where F is the Jacobian (linear approximation) of f at time $k-1$, Q is the covariance of the model associated with state $\hat{x}_{k-1}$, and superscript T denotes matrix transposition, .

The update step, which is carried out when a new observation z_k is available at time k, provides a final estimate (posterior) of $\hat{x}_k$ by means of the following expressions:

$$K_k = P_k H^T (HP_k H^T + R_k)^{-1}, \tag{3}$$

$$\hat{x}_k = \hat{x}_k + K_k(z_k - h(\hat{x}_k)), \tag{4}$$

$$P_k = (I - K_k H)P_k. \tag{5}$$

Here, h symbolically denotes the observation model, which relates the state variable to the measurement(s) z_k, and H corresponds to its linear approximation at time k. Note that z_k may correspond either to a single measured feature or to a set of features (e.g. backscattering coefficient at various channels). Further details of the observation model are provided in Subsection II-C2. Variable K_k corresponds to the Kalman gain at time k, and it is a critical component of the filter since it determines how much weight is given to the measurement versus the prior. The value of the Kalman gain depends on the model covariance Q (Eq. 2) and the covariance of the observation R. The final estimate $\hat{x}_k$ in Eq. 4 and its uncertainty P_k (Eq. 5) are recursively updated as a function of K_k. It is very important to note that the Kalman gain is dynamically (i.e., temporally) adapted based on the uncertainties (in terms of the covariances) of both the evolution and observation models, making the filter robust to varying uncertainty (i.e., noise) levels and, simultaneously, ensuring that an optimal estimate is delivered.

1) Evolution Model: The evolution model describes how the state variable changes over time and is used in the prediction step of the Kalman filter to generate an a priori estimate, as previously mentioned. This evolution is represented with a symbolic or generic function f as shown with Eq. 1. It is worth noting that, in our case, an analytical expression for f is normally not available, either because it does not exist or would be extremely complex. The evolution model could be derived from crop growth models such as WOFOST [35] or DSSAT [36], among others. However, after some testing we concluded that they cannot replicate the variability observed in our study case (Fig. 2). Consequently, we decided to extract temporal dynamics directly from the data gathered in the field campaign.

Several approaches can be used to obtain an empirical expression of f, such as curve-fitting methods (e.g., polynomial models) or machine learning regression techniques. Such methods tend to provide an average response for each date along the growing season, as well as smooth variations. Therefore, they cannot follow the quick changes and strong variability observed in the biomass for the measured points, and, consequently, they would inevitably introduce bias in the estimations if such methods were applied (estimations would be biased towards the average of all curves). For this reason, we opted instead to employ *transition matrices*, modeling the biomass temporal evolution as a first-order discrete-time Markov process (or chain) [37]. In such a model, the state space is defined as a set of possible (i.e., discrete) biomass levels, and temporal dynamics are described by the transition probabilities between these states.

Formally, we model the biomass as a discrete random variable $\hat{x} : \Omega \to S$, being S a numerable set representing the state space of the process, and each $s \in S$ is a state (that is, we assume that the values Ω of the state variable $\hat{x}$ belong to a set of possible discrete values or 'bins'). We also assume that the value $\hat{x}_k$ verifies the Markov condition, so that it depends only on $\hat{x}_{k-1}$ (i.e., the estimated biomass at discrete time k depends solely on the previous estimate at time $k-1$, and not on any earlier values). That is, the probability of moving to a next state j depends only on the current state i:

$$P_{ij}(k) = P(\hat{x}_k = j \mid \hat{x}_{k-1} = i) \tag{6}$$

for all $k \geq 0$, $i, j \in S$. The Markov process is described with a square matrix $\mathbf{\Gamma}_k$ denoted as transition matrix, which contains the probabilities of moving to each state from any individual state for every discrete time k. It is very important to note that we define a transition matrix for every time k, which means that the transition probabilities change over time. This corresponds to a time-inhomogeneous Markov chain, which is represented by a sequence of transition matrices $\mathbf{\Gamma}_k$. Such formulation allows us to model biomass dynamics in two dimensions, incorporating both the biomass values and the temporal information provided by the Day of Season (DoS).

Assuming that there are $N \in \mathbb{N}^+$ possible states, each $\mathbf{\Gamma}_k$ is a $N \times N$ matrix defined as:

$$\mathbf{\Gamma}_k = \begin{bmatrix} P_{1,1}(k) & P_{2,1}(k) & ... & P_{N,1}(k) \\ P_{1,2}(k) & P_{2,2}(k) & ... & P_{N,2}(k) \\ \vdots & \vdots & \vdots & \vdots \\ P_{1,N}(k) & P_{2,N}(k) & ... & P_{N,N}(k) \end{bmatrix} \tag{7}$$

Each column of $\mathbf{\Gamma}_k$ contains the probabilities $P_{ij}(k)$ of transitioning from current state i to future state j at time k (see Eq. 6). Evidently, each $\mathbf{\Gamma}_k$ satisfies the following conditions concerning probabilities:

$$P_{ij}(k) \in [0, 1], \forall i, j \in S, \tag{8}$$

$$\forall i \in S, \sum_{j \in S} P_{ij}(k) = 1. \tag{9}$$

that is, each probability $P_{ij}(k)$ lies between 0 and 1, and the summation of all probabilities of moving from state i to j at time k is 1. This matrix $\mathbf{\Gamma}_k$ allows us to calculate the most probable future state and its associated variance (i.e., uncertainty) Q (see Eq. 2) required for the application of the KF. The most probable state provided by the evolution model (the prior in Eq. 1) is:

$$\hat{x}_k = \arg\max_j P_{ij}(k) \tag{10}$$

and the variance is:

$$\begin{aligned} Q_k &= \mathrm{Var}[\hat{x}_k = j \mid \hat{x}_{k-1} = i] \\ &= \sum_{j=1}^{N} \hat{x}_j^2 \, P_{ij}(k) - \left(\sum_{j=1}^{N} \hat{x}_j \, P_{ij}(k) \right)^2 \end{aligned} \tag{11}$$

where $\hat{x}_j$ corresponds to the numeric value associated with future state j. Since no analytical function is used, Eq. 2 simplifies to:

$$P_k = P_{k-1} + Q_k \tag{12}$$

For practical purposes, we decided to generate weekly transitions so that each $\mathbf{\Gamma}_k$ captures how likely it is for biomass to change from one state to another between week $k-1$ and k. Daily transitions are not considered, as significant crop variations over a single day are negligible, and because ground truth measurements are available at weekly/biweekly intervals. In this way, aligning the model with this temporal resolution provides more consistent and meaningful estimates.

Figure 3 shows examples of transition matrices generated for biomass at DoS 10, 100, and 200. There is a total of 132 possible states, being each one associated with a specific discrete interval of biomass values. As shown in (7), each element of the matrix contains the probabilities of transitioning from a current state (horizontal axis of Fig. 3) to a future state (vertical axis). For instance, and to illustrate the use of this matrix, in the magnified image of Fig. 3(a), the green and red rectangles highlight the case where, at $DoS = 10$, the current biomass state is $i = 12$. In this situation, there are ten possible future states (red rectangle), each associated with a probability. The non-zero probabilities are listed in Table II, which shows that a transition to state 14 is the most probable. Accordingly, we deduce that at $DoS = 10$, if the current state is $i = 12$, the future state (one week ahead) is $j = 14$ (which corresponds to a biomass value of 0.015 kg.). Also, by means of Eq. 11, we can derive the variance of the estimation which is approximately $Q_{k=10} = 0.000014$ kg^2.

2) Observation Model: The observation model provides estimates of the crop physical variable as a function of the different satellite observations. As noted earlier, we use time series of Sentinel-1 and Sentinel-2 imagery. Both SAR- and optical-based observation models were generated using the Random Forest Regressor (RFR), provided by the *scikit-learn* package in Python language [38]. Therefore, as with the evolution model, we do not employ an analytical function for h (see Eq. 4), so that the posterior (i.e., the final estimate after the update step) directly depends on the output of the RFR and

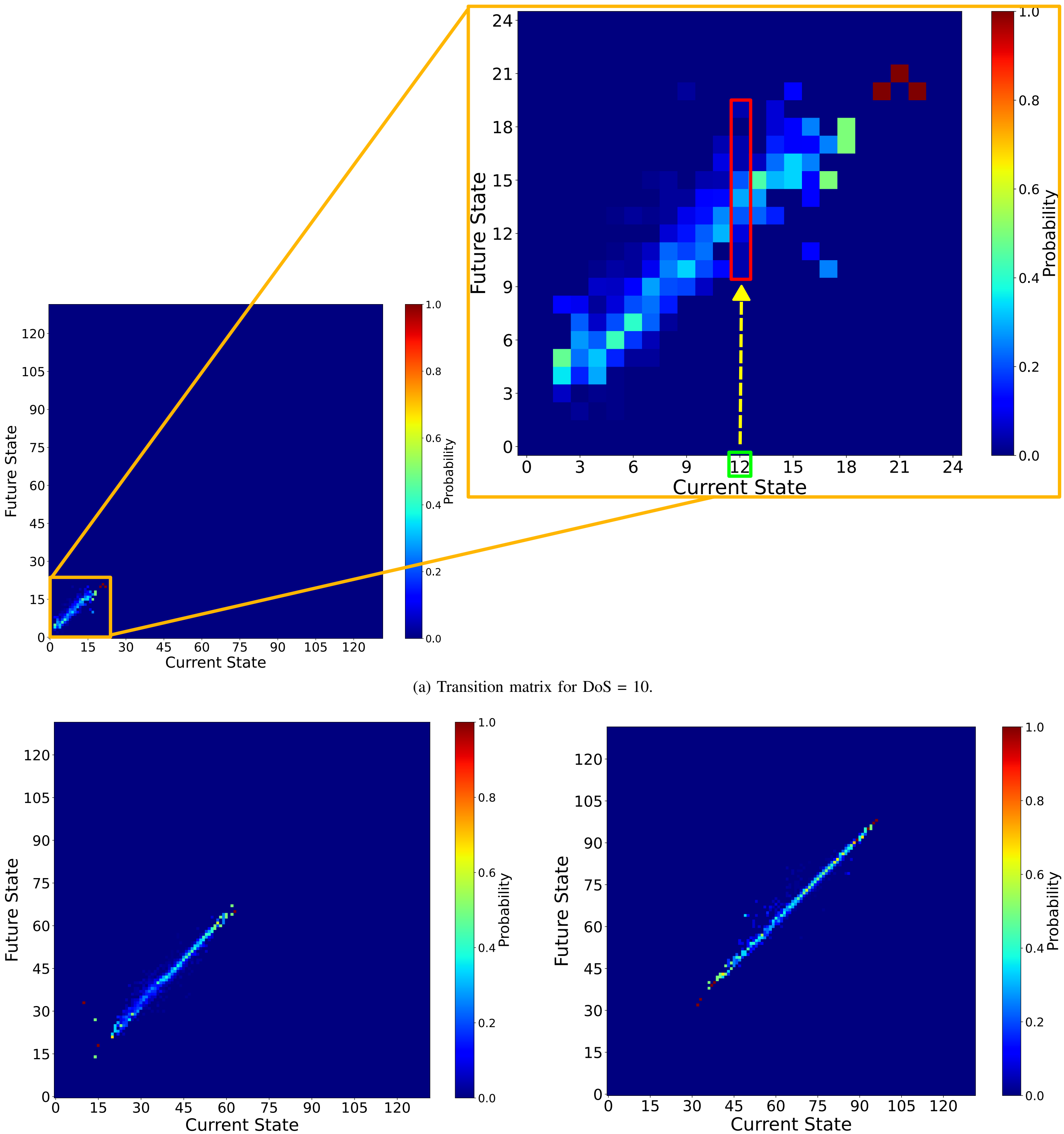

(a) Transition matrix for DoS = 10.

(b) Transition matrix for DoS = 100.

(c) Transition matrix for DoS = 200.

Fig. 3. Example of transitions matrices for three different dates.

the Kalman gain. In this regard, Eq. 3 can be simplified to its scalar version:

$$K_k = \frac{P_k}{P_k + R_k}, \tag{13}$$

where R_k (uncertainty of the observation) is calculated as the variance across all trees of the RFR. The final uncertainty of the model (Eq. 5) is also simplified to:

$$P_k = (1 - K_k)P_k. \tag{14}$$

For the SAR model, multiple features derived from the original images can be employed, including backscatter and interferometric coherence at diverse polarimetric channels. An ablation study analyzing the contribution of the different SAR features is presented in Section III-C. The optical model relies

TABLE II
EXAMPLE OF USE OF TRANSITION MATRIX.

Current state	Current value	Future state	Future values	Probability
12	0.005	10	0.007	0.04
		11	0.009	0.04
		12	0.011	0.08
		13	0.013	0.21
		14	**0.015**	**0.29**
		15	0.017	0.21
		16	0.019	0.04
		17	0.021	0.04
		18	0.023	0.01
		19	0.025	0.04

solely on NDVI measurements. Additionally, the day of season (DoS) was included as an input feature for both SAR and optical models to better capture crop growth dynamics.

To train the two models, the datasets are split into training and testing sets using, respectively, 70% and 30% of the available data. The number of trees of the RFR is set to 300.

The performance of the SAR and optical observation models is evaluated by comparing estimated and observed biomass values, as illustrated in the scatter plots of Fig. 4. Although the same percentage of testing samples is to create both models, Figs. 4(a) and (b) highlight that the absolute number of testing samples is lower for the optical case, due to the reduced availability of cloud-free images in the area. For this case, the SAR observation model comprises backscatter and interferometric coherence of both polarimetric channels (i.e. four features).

Quantitatively, the performance of each observation model is evaluated using the root mean squared error (RMSE) and the mean absolute error (MAE) between estimated and true biomass values, as summarized in Table III. These metrics indicate that the SAR model performs worse than the optical model, with higher RMSE and MAE values (0.29 kg and 0.20 kg, respectively). In contrast, the optical model achieves lower errors (a RMSE of 0.23 kg and a MAE of 0.15 kg), reflecting its greater sensitivity to biomass.

TABLE III
SAR AND OPTICAL OBSERVATION MODELS GLOBAL ACCURACY METRICS FOR BIOMASS ESTIMATION.

	RMSE [kg]	MAE [kg]
SAR observation model	0.283	0.194
Optical observation model	0.232	0.157

3) Algorithm Workflow: Taking into account the previously defined evolution and observation models, Fig. 5 shows how the complete integration algorithm proceeds to provide biomass estimates throughout the season.

As described in Subsection II-C1, the transition matrices are defined on a weekly basis, enabling the evolution model to generate an estimate (provided by the prediction step of the Kalman filter) at weekly intervals. Subsequently, different scenarios are considered depending on the availability of satellite observations acquired during the week for which the biomass value is to be estimated:

1) **Case 1: No observation** - The final estimate corresponds to the one provided by the evolution model (there is no update step in the KF).
2) **Case 2: Sentinel-1 observation** - When a Sentinel-1 image is available, the estimate is updated using the SAR observation model.
3) **Case 3: Sentinel-2 observation** - When a Sentinel-2 image is available, the estimate is updated using the optical observation model.
4) **Case 4: Sentinel-1 and Sentinel-2 observations** - When both images are available, the estimate is updated using both observation models.

D. Evaluation

Model performance is assessed by the Root Mean Square Error (RMSE) and Mean Absolue Error (MAE), widely employed for estimation tasks in a variety of areas. Moreover, we include an additional and specific quantitative quality metric which is the difference in accumulated biomass between the estimations and the ground data.

Essentially, accumulated biomass represents the total biomass produced by one plant over the growing season and can be defined as:

$$B_{acc} = \int_{t_0}^{t_f} B(t)\,dt \tag{15}$$

being B_t the biomass at time t, t_0 and t_f correspond to the first and last day of the growing season. It is therefore the area under the biomass–time curve. The difference of accumulated biomass $\bar{B}_{acc}$ is defined as:

$$\bar{B}_{acc} = |\hat{B}_{acc} - B_{acc}|. \tag{16}$$

where $\hat{B}_{acc}$ results from the accumulation of estimated value and B_{acc} is the accumulation of in-situ measured values.

III. RESULTS

A. Detailed Results at Selected Points

The proposed integration approach is applied to estimate weekly biomass values throughout a complete season of sugarcane crops. To correctly evaluate the methodology, we start by making a selection of the measurement points (with available ground-truth data) to build both the evolution and observation models. Specifically, we employ 90% of the points (63 from a total of 70 points) to build the models, and the remaining 10% (7 points) are reserved for testing and validating. In this way, all data associated with the testing points are not 'seen' by the models. Evidently, in all cases, biomass estimates are compared with the in-situ data collected during the field campaign.

As explained in Section II-C, the proposed methodology combines temporal crop dynamics with SAR and optical observations, resulting in a complete integration framework. The results presented in this section correspond to the case in which all available SAR products are employed as input features to

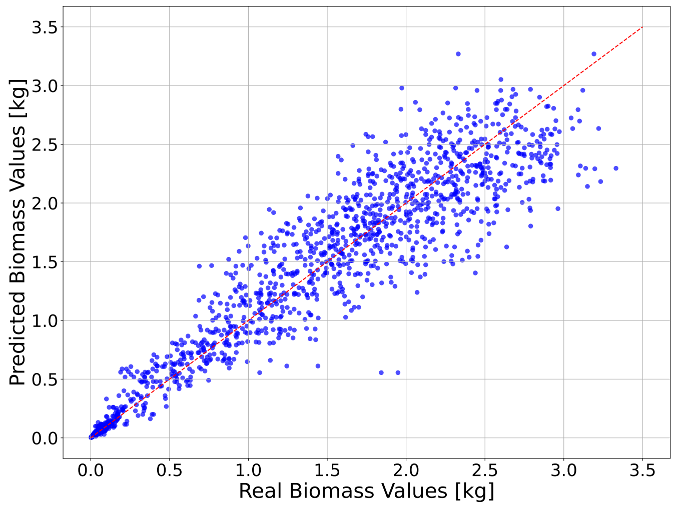

(a) SAR observation model accuracy.

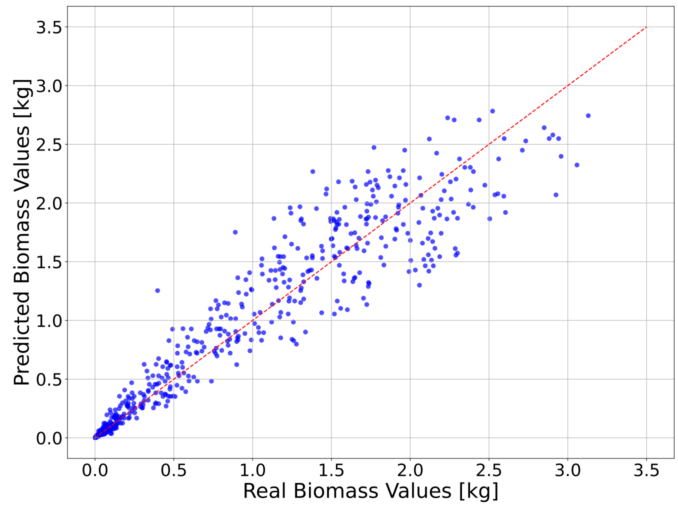

(b) Optical observation model accuracy.

Fig. 4. Accuracy assessment of SAR and optical models in terms of estimated versus real biomass values.

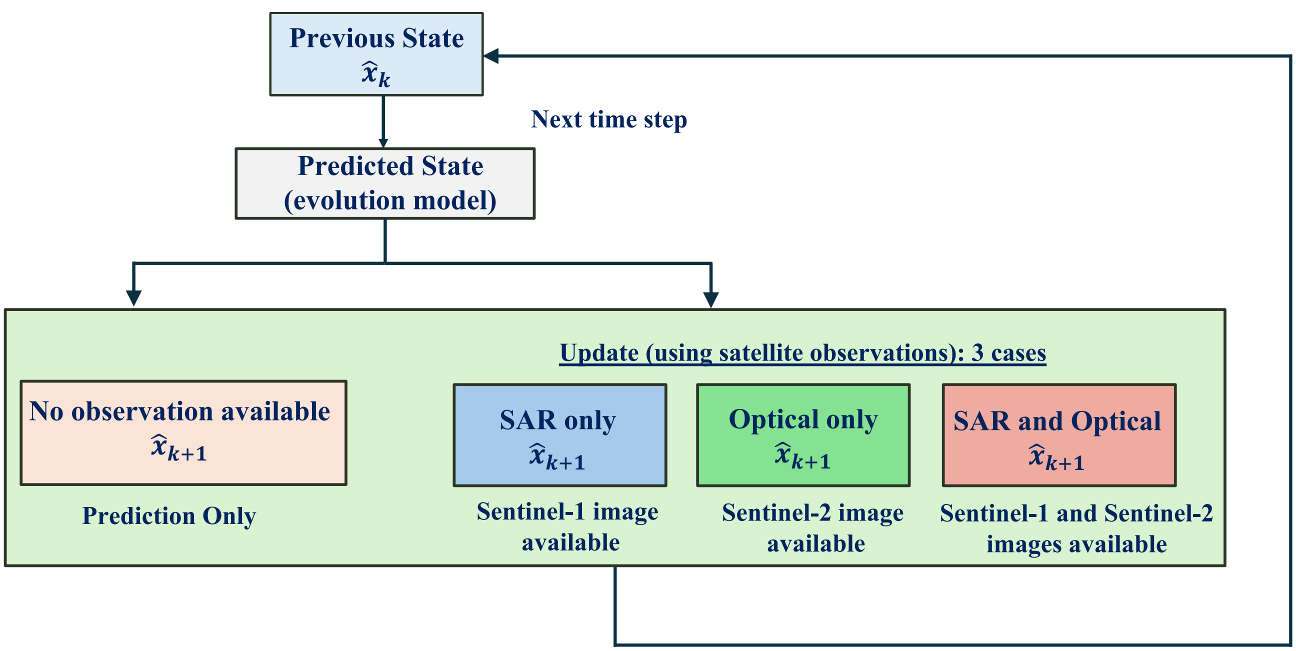

Fig. 5. Workflow of the proposed integration algorithm.

the RFR. This means that the inputs to the the SAR observation model are VH and VV backscattering coefficients, VH and VV coherences, and DoS, whereas the optical observation model relies on NDVI and DoS as inputs.

To better assess the contribution of the proposed method, we also compare its performance with several alternative approaches that could have been adopted. As a first group of alternatives, we test three methods that do not incorporate any form of integration, i.e. they rely exclusively on satellite imagery and machine learning. Furthermore, a second group consists of two methods based on partial integration of satellite observations, in which the prediction step is followed by an update step using either only SAR or only optical imagery (but not both simultaneously).

We begin by presenting the results shown in Fig. 6, which correspond to weekly biomass estimates over an entire growing season for five different points. They were selected as representative of some behaviours relevant to be considered in this analysis. It is important to remind that all the data of these points (i.e., in-situ measured biomass as well as SAR and NDVI values) were not used in the construction of the evolution and the observation models. As shown in Figs. 6(a)–(e), the estimated biomass values (blue dots) exhibit good overall agreement with the ground-truth measurements (green dots). Notably, nearly all estimates lie within the interval defined with $\pm$ one standard deviation, showing another positive indicator of model reliability.

An important aspect is that the integration algorithm can correctly track abrupt biomass changes that happen across the season. For instance, as shown in Fig. 6(b) for farm El Trejo (point 34), there is an important drop in the biomass between approximately DoS 160 and 180, followed by a consistent increase until DoS 300. A sudden drop is also observed in Fig. 6(e) for farm El Faro Empresa (point 11) around DoS 250, followed by an increase until the end of season. In both cases, the proposed integrated model successfully reproduces these decreases and subsequent recoveries in biomass. Such a predictive accuracy would be challenging to achieve using alternative approaches based on regressions (curve fitting), which typically capture only general trends rather than abrupt temporal changes. It is worth mentioning that these fluctuations in biomass are probably caused by leaf senescence. As the crop canopy matures, older lower leaves naturally die and dry out, reducing the amount of green and total biomass. This drop is part of the normal growth cycle, as the plant reallocates nutrients from aging leaves to support the development and thickening of the stalks. Subsequently, biomass increases again as growth continues.

Furthermore, by comparing Figs. 6(d) and (e), we observe that, although both points belong to the same field, they exhibit very different temporal biomass patterns, with point 11 producing more biomass than point 12 (approximately 1 more kilogram at the end of the season). However, in both cases, the algorithm accurately captures these differences without introducing a bias, demonstrating that the model is well-adapted to the strong variability present in the scene, as mentioned in Section II-A and shown in Fig. 2(b).

Quantitative metrics for these five points are detailed in Table IV. Both the RMSE and MAE values are very, on the order of a hundred of grams for plants producing between 1.5 kg and 3 kg of biomass. Also, the difference is accumulated biomass is generally low which indicates that the method provides reliable estimates over the whole growing season.

The proposed methodology allows us to integrate as many types of observations as desired. In our case, we consider SAR and optical imagery, but the same approach could be followed using only SAR or only optical data, resulting in a partial integration of all available satellite observations. Figure 7 shows the biomass estimation results with partial integration for the same points as the ones shown in Fig. 6. The general trends of the biomass temporal evolution are correctly retrieved using only either SAR or optical images (red and orange dots respectively). However, more fluctuations (and deviations from the in-situ data) are observed in the estimates for both cases compared to the complete integration case (Fig. 6). For instance, this can be observed between DoS 150 and 250 for point 12 (Fig. 7(e)). Also note how the standard deviation of the estimates are consistently larger than when both types of observations (SAR and optical) are considered, showing that the uncertainty of the resulting estimates increases. Moreover, we see in Fig. 7(e) that the estimates derived from SAR data are more adjusted to the in-situ data than the ones derived from optical data, especially at DoS 300–340.

Quantitative results for these five points using a partial integration of satellite imagery are summarized in Table V. There is a general decrease in accuracy, with increased RMSE, MAE and accumulated biomass difference, compared to the complete integration approach. When comparing the partial integration based on SAR against the one based on NDVI, the radar case provides better results (lower error metrics). This is probably due to the larger number of valid images (as they are not affected by clouds), which allows the integration algorithm to track more frequently, hence better, the biomass evolution than in the optical-only case.

The accuracy of the proposed integration algorithm is also evaluated against models that rely on pure machine learning and satellite observations. It is important to note that artificial intelligence (AI) methods are widely used in agricultural applications involving remote sensing data, such as yield prediction or crop phenology retrieval, among others. Therefore, it is essential to test the scenario where biomass is estimated using only observations and such methods.

Similar to the previous approach, different cases are considered. In the first case, biomass estimation is based exclusively on SAR data, using all available SAR products and the DoS as input features. In the second case, biomass estimation relies solely on NDVI and the DoS. Finally, in the third case, both data sources are combined, so that biomass estimates are produced using either SAR or NDVI data, depending on the availability of each type of image during the week the estimation is performed. When both a SAR and an optical image are available, the final biomass estimate and its uncertainty correspond to the average of both models.

The resulting weekly biomass estimates for the same test points shown in Fig. 6 are displayed in Fig. 8. As observed, the overall accuracy decreases across all cases, regardless of whether biomass estimates are based solely on SAR data, NDVI, or a combination of both. Noticeable fluctuations are evident, particularly in the estimates relying only on SAR data, as illustrated in Fig. 8(e) between DoS 270 and 350. In addition, an extreme example highlighting the limitations of optical data due to cloud cover is shown in Fig. 8(a), where biomass estimates remain constant from DoS 250 to the end of season (DoS 350) because of the absence of available optical imagery. Furthermore, the estimation uncertainty is noticeably higher in all three cases, as indicated by the wider shaded areas representing one standard deviation of each model estimates.

B. Overall Results

Besides presenting estimation results for specific points, Table VII summarizes the overall accuracy of the proposed integrated model and the alternative approaches previously described, in terms of average RMSE, MAE, and accumulated

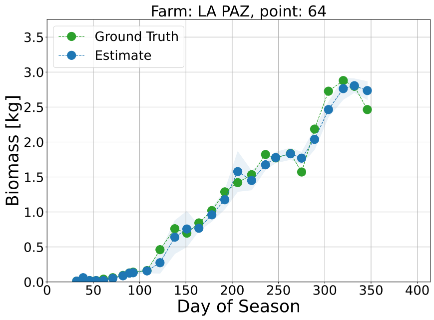

(a) Point 64 of 70 (farm La Paz).

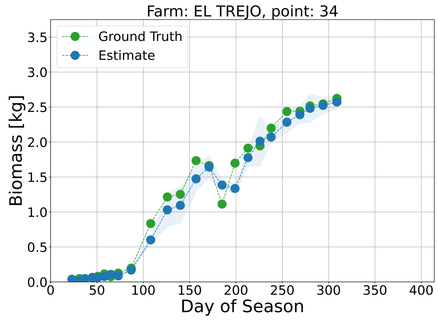

(b) Point 34 of 70 (farm El Trejo)

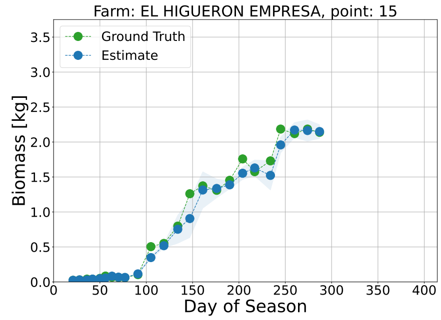

(c) Point 15 of 70 (farm El Higuerón Empresa)

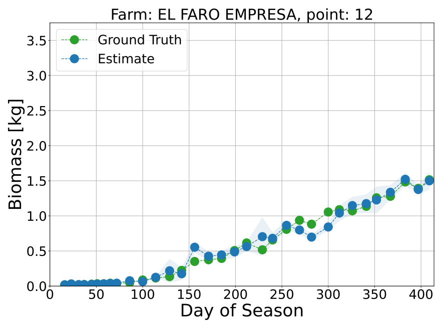

(d) Point 12 of 70 (farm El Faro Empresa)

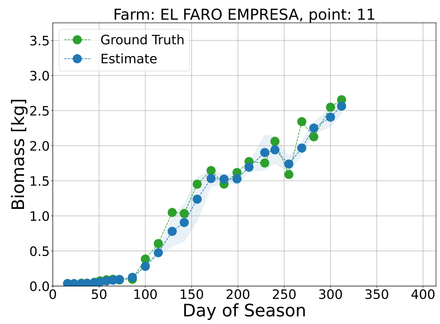

(e) Point 11 of 70 (farm El Faro Empresa)

Fig. 6. Temporal evolution of biomass estimates and in-situ measured biomass throughout a complete season for five different points with the proposed integration algorithm. The shaded blue area represents ± one standard deviation of the model estimates.

TABLE IV
QUANTITATIVE ACCURACY METRICS FOR FIVE POINTS WITH A COMPLETE INTEGRATION OF SATELLITE OBSERVATIONS.

	Testing Point					Average
	64	34	15	12	11	
RMSE [kg]	0.113	0.138	0.112	0.130	0.079	**0.103**
MAE [kg]	0.077	0.097	0.066	0.093	0.052	**0.072**
True Accumulated Biomass [kg·day]	382.6	391.0	281.4	241.9	355.0	
Estimated Accumulated Biomass [kg·day]	371.0	367.2	264.7	243.7	336.9	
Accumulated Biomass Difference [kg·day]	11.5	23.8	16.7	1.8	18.1	**14.4**

biomass difference. Note that maximum values of these three metrics are also detailed. The same procedure is followed, where 90% of the points (63) are used for model construction and 10% (7) for validation. However, the metrics shown in Table VII correspond to values computed over 100 iterations of randomly selecting the points (i.e., each model is applied 700 times in total). It is important to note that the random selection in each iteration is precomputed so that the same training and validation points are used consistently across all models. As can be observed from Table VII, the proposed fully integrated approach achieves the highest accuracy, yielding the lowest RMSE, MAE, and accumulated biomass difference on average. In addition, maximum errors are consistently lower, showing that the model is better adapted to all possible scenarios (i.e., for low or high biomass productivity points). Thus, the complete integration algorithm demonstrates superior estimation performance compared to all alternative methods.

Partial integration using only SAR or NDVI improves accuracy relative to the observation-only ML models but still results in higher errors. Machine learning approaches relying exclusively on satellite imagery —whether SAR, NDVI, or their combination— consistently perform worse than the integrated methods. It is also worth noting that, in this study, models based solely on optical data (NDVI) exhibit the lowest accuracy, likely due to the significant lack of usable images caused by cloud cover in the Cauca Valley. Consequently, incorporating SAR data proves essential for effective crop monitoring in this region.

C. Ablation Study

To further evaluate the proposed methodology, we conducted an ablation study focusing on the contribution of SAR imagery in the integrated model. Unlike optical data, SAR images are consistently acquired over the study area, regardless of cloud cover or other atmospheric conditions. This ensures

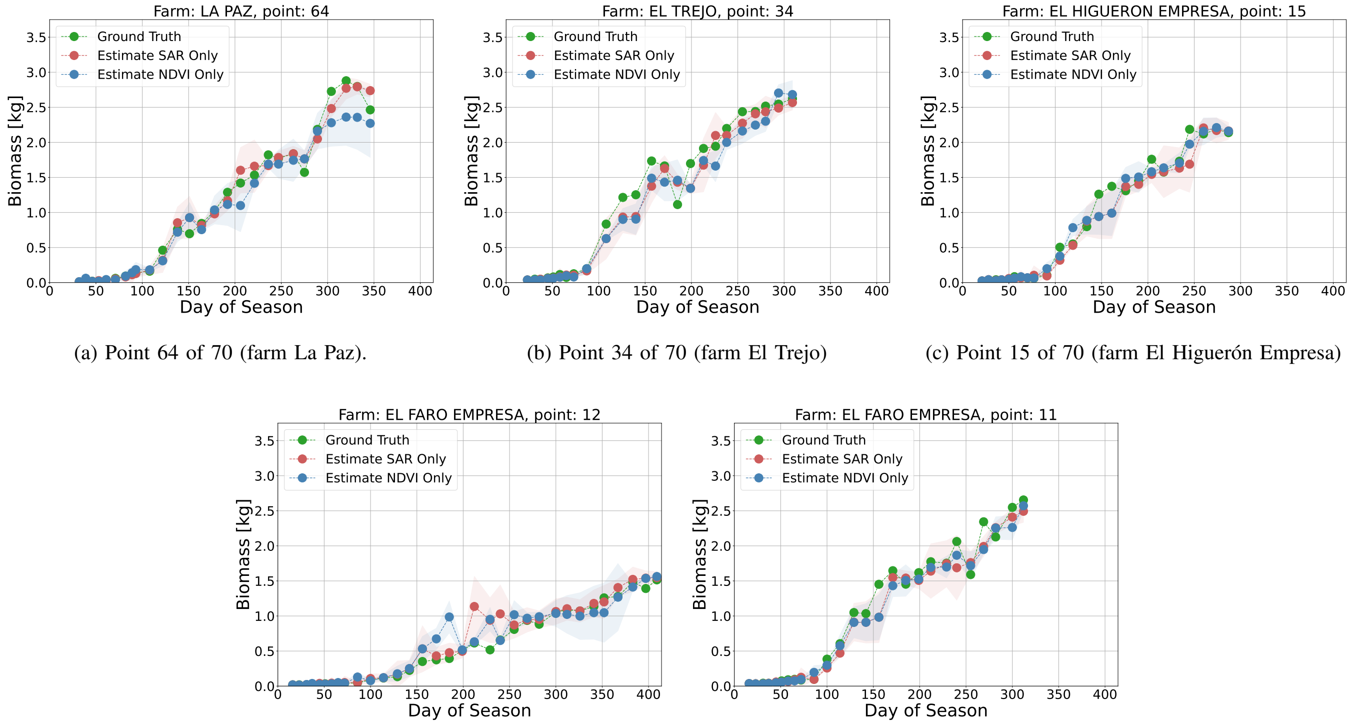

(a) Point 64 of 70 (farm La Paz). (b) Point 34 of 70 (farm El Trejo) (c) Point 15 of 70 (farm El Higuerón Empresa)

(d) Point 12 of 70 (farm El Faro Empresa) (e) Point 11 of 70 (farm El Faro Empresa)

Fig. 7. Temporal evolution of biomass estimates and in-situ measured biomass throughout a complete season for five different points with the integration algorithm using either only SAR or only optical imagery (partial integration). The shaded area represents ± one standard deviation of the model estimates.

TABLE V
QUANTITATIVE ACCURACY METRICS FOR FIVE POINTS WITH A PARTIAL INTEGRATION OF SATELLITE OBSERVATIONS.

	Testing Point					**Average**
	64	34	15	12	11	
RMSE - SAR Only [kg]	0.119	0.172	0.159	0.144	0.164	**0.137**
MAE - SAR Only [kg]	0.082	0.121	0.090	0.072	0.110	**0.091**
RMSE - NDVI Only [kg]	0.193	0.201	0.137	0.157	0.159	**0.189**
MAE - NDVI Only [kg]	0.126	0.157	0.087	0.085	0.106	**0.135**
True Accumulated Biomass [kg·day]	382.6	391.0	281.4	241.9	355.0	
Estimated Accumulated Biomass - SAR Only [kg·day]	368.7	362.0	260.7	273.4	328.9	
Estimated Accumulated Biomass - NDVI Only [kg·day]	350.5	353.1	264.0	265.8	329.4	
Accumulated Biomass Difference - SAR Only [kg·day]	13.8	29.0	20.7	31.4	26.1	**24.2**
Accumulated Biomass Difference - NDVI Only [kg·day]	32.0	37.9	17.4	23.8	25.6	**27.4**

that the time series of backscatter and coherence (for both VV and VH polarizations) are complete and free of gaps. Therefore, we trained the RFR used in the SAR observation model with different combinations of SAR-derived features and assessed the overall performance of the integration algorithm for each case. In other words, we tested how the approach performs when using various subsets of SAR features in the observation model, while the final estimates still rely on the Kalman filter–based integration of expected evolution and satellite observations.

The different sets of input features considered in this study are summarized in Table VIII. First, multiple configurations employing single-polarimetric features were defined (sets 2, 3, 7, and 8), including either the backscatter intensity at a single polarization (VH or VV) or the combination of intensity and coherence at the corresponding polarization channel. Second, the effect of incorporating dual-polarimetric information from both VH and VV channels was examined (sets 4, 5, and 6). In this context, the contribution of the Radar Vegetation Index (RVI), defined as the ratio between VH and VV backscatter intensities, is also evaluated:

$$\mathrm{RVI} = \frac{4\mathrm{VH}}{\mathrm{VH} + \mathrm{VV}}. \tag{17}$$

The final set (Set 9) incorporates all available SAR features (i.e., VH and VV backscatter and coherence), and represents the optimal model, the results of which were presented in Section III.

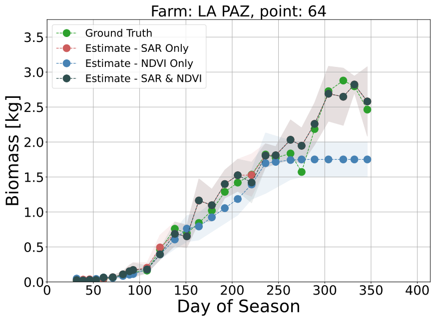

(a) Point 64 of 70 (farm La Paz).

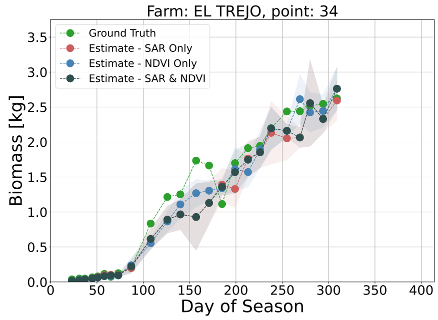

(b) Point 34 of 70 (farm El Trejo)

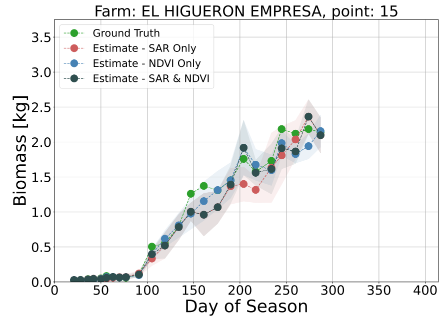

(c) Point 15 of 70 (farm El Higuerón)

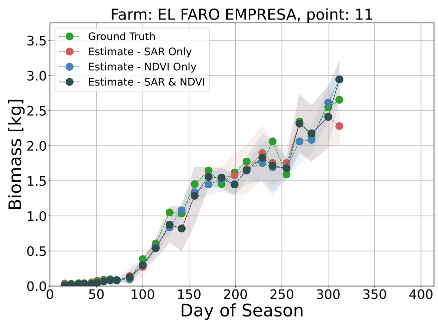

(d) Point 11 of 70 (farm El Faro Empresa)

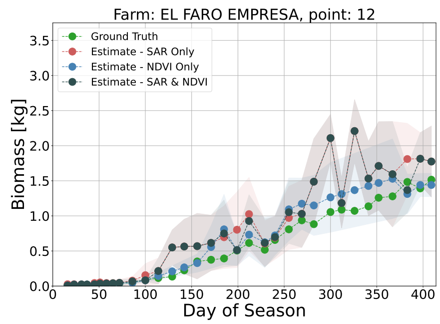

(e) Point 12 of 70 (farm El Faro Empresa)

Fig. 8. Temporal evolution of biomass estimates and in-situ measured biomass throughout a complete season for five different points using only satellite observations (SAR, optical, or both simultaneously) and machine learning.

TABLE VI
QUANTITATIVE ACCURACY METRICS FOR FIVE POINTS USING ONLY SATELLITE OBSERVATIONS WITH A MACHINE LEARNING APPROACH.

	Testing Point					Average
	64	34	15	12	11	
RMSE - SAR Only [kg]	0.121	0.272	0.173	0.364	0.132	**0.212**
RMSE - NDVI Only [kg]	0.396	0.194	0.126	0.161	0.134	**0.202**
RMSE - SAR and NDVI [kg]	0.123	0.256	0.147	0.357	0.126	**0.202**
MAE - SAR Only [kg]	0.076	0.181	0.112	0.241	0.092	**0.140**
MAE - NDVI Only [kg]	0.221	0.137	0.079	0.111	0.090	**0.127**
MAE - SAR and NDVI [kg]	0.081	0.168	0.093	0.223	0.091	**0.131**
True Accumulated Biomass [kg·day]	382.6	391.0	281.4	241.9	355.0	
Estimated Accumulated Biomass - SAR Only [kg·day]	397.8	337.4	250.3	352.8	339.0	
Estimated Accumulated Biomass - NDVI Only [kg·day]	312.5	358.0	265.6	285.9	337.1	
Estimated Accumulated Biomass - SAR and NDVI [kg·day]	395.4	344.1	260.5	341.4	338.3	
Accumulated Biomass Difference - SAR Only [kg·day]	15.3	53.5	31.1	110.9	16.0	**45.4**
Accumulated Biomass Difference - NDVI Only [kg·day]	70.0	33.0	15.8	44.0	17.9	**36.1**
Accumulated Biomass Difference - SAR and NDVI [kg·day]	12.8	46.9	20.9	99.4	16.6	**39.3**

TABLE VII
GLOBAL ACCURACY METRICS OBTAINED WITH THE PROPOSED INTEGRATION ALGORITHM AND WITH ALTERNATIVE APPROACHES, AFTER 100 ITERATIONS OF RANDOMLY-SELECTED POINTS.

Method	**RMSE [kg]**	**MAE [kg]**	**Accumulated Biomass Difference [kg·day]**
Partial Integration - SAR only	0.132 (Max.: 0.214)	0.087 (Max.: 0.126)	18.2 (Max.: 32.9)
Partial Integration - NDVI only	0.168 (Max.: 0.268)	0.119 (Max.: 0.171)	22.2 (Max.: 39.4)
Observation only (ML) - SAR	0.153 (Max.: 0.364)	0.099 (Max.: 0.241)	29.4 (Max.: 110.9)
Observation only (ML) - NDVI	0.189 (Max.: 0.414)	0.101 (Max.: 0.259)	33.4 (Max.: 80.0)
Observation only (ML) - SAR + NDVI	0.150 (Max.: 0.349)	0.098 (Max.: 0.227)	31.1 (Max.: 96.4)
Proposed - Complete Integration	**0.103 (Max.: 0.155)**	**0.064 (Max.: 0.091)**	**13.8 (Max.: 25.3)**

TABLE VIII
SELECTED INPUT FEATURES TO TRAIN THE RFR FOR THE SAR OBSERVATION MODEL.

Set Number	Input Features	Information Type
Set 1	DoS	Temporal
Set 2	VH, DoS	Single-pol intensity, temporal
Set 3	VV, DoS	Single-pol intensity, temporal
Set 4	VH, VV, DoS	Dual-pol intensity, temporal
Set 5	RVI, DoS	Dual-pol intensity, temporal
Set 6	VH coherence, VV coherence, DoS	Dual-pol interferometry, temporal
Set 7	VH, VH coherence, DoS	Single-pol intensity, interferometry, temporal
Set 8	VV, VV coherence, DoS	Single-pol intensity, interferometry, temporal
Set 9 - Full Model	VH, VV, VH coherence, VV coherence, DoS	Dual-pol intensity, interferometry, temporal

Accuracy metrics are summarized in Table IX, with the results of the best-performing model (Set 9) repeated for easier comparison. Following the same validation procedure used for the integration approaches presented in Table VII of Section III, 90% of the measured points are randomly selected for model construction, and the remaining 10% are used for validation. This process is repeated 100 times to provide a more reliable evaluation of the performance achieved with each set of SAR features.

Using only temporal information (DoS, Set 1) results in the highest errors: RMSE is 0.194 kg (Max: 0.568), MAE is 0.137 kg (Max: 0.378), and accumulated biomass difference is, on average, 43.791 kg·day (Max: 175.732). When any of the available SAR features are included in the observation model, an improvement is clearly observed, which demonstrates that SAR data provide sensitivity to sugarcane biomass. In this regard, including traditional VH and VV backscatter intensities as input features significantly reduces the errors, with VH slightly outperforming VV when used individually. For VH backscatter (Set 2), a RMSE of 0.109 kg (Max: 0.265), a MAE of 0.074 kg (Max: 0.143), and an average accumulated biomass difference of 16.858 kg·day (Max: 47.199). Using VV intensity (Set 3) yields slightly higher errors: RMSE is 0.115 kg (Max: 0.288), MAE is 0.108 kg (Max: 0.162), and accumulated biomass difference is 23.261 kg·day (Max: 51.026). However, combining both VH and VV intensities (Set 4) reduces errors further: RMSE = 0.108 kg (Max: 0.181), MAE = 0.071 kg (Max: 0.127), and accumulated biomass difference becomes 15.692 kg·day (Max: 31.913). Set 5, based on the RVI, which directly depends on both VH and VV intensities, shows similar performance to Set 4 (RMSE = 0.108 kg (Max: 0.175), MAE = 0.070 kg (Max: 0.121), and accumulated biomass difference is 15.748 kg·day (Max: 30.856)).

As also shown in Table IX, using only the interferometric coherence (Set 6) of both polarizations results in a drop in accuracy: RMSE = 0.125 kg (Max: 0.307), MAE = 0.081 kg (Max: 0.174), and accumulated biomass difference = 27.034 kg·day (Max: 56.554), likely due to temporal decorrelation effects.

Furthermore, an important point is that combining intensity and coherence features (Sets 7 and 8) substantially improves performance. Set 7, based only on VH polarization data, achieves a RMSE of 0.104 kg (Max: 0.164), a MAE of 0.068 kg (Max: 0.114), and an accumulated biomass difference of 14.012 kg·day (Max: 27.323). Set 8, using only VV intensity and coherence, reaches similar accuracy with a RMSE of 0.105 kg (Max: 0.169), a MAE of 0.069 kg (Max: 0.118), and an accumulated biomass difference of 14.136 kg·day (Max: 28.762). These results indicate that intensity and coherence provide complementary information that can be jointly exploited for biomass estimation using the proposed methodology. Also, from Table IX, we deduce that there is no large difference in performance between jointly using as input features intensity and coherence data acquired at both VH and VV polarizations (Set 9, the best-performing model), and using only intensity and coherence features at a single polarimetric channel (Sets 7 and 8). This is particularly relevant if the proposed methodology is implemented using SAR data acquired by a sensor without polarimetric capabilities (i.e., single-pol). The reason for the excellent performance when both intensity and coherence are jointly exploited may stem from the complementary information they provide, as these two features are sensitive to different properties of the scene, as analysed in [39] for a wide variety of crop types. In such a case, even working with a single channel (VV or VH) the time series of radar features are very informative about the crop growth.

Beyond overall accuracy metrics, the influence of different input features on biomass predictions becomes clearer when examining results at some specific points. Figure 9 illustrates the temporal evolution of biomass estimates for point 15 using different subsets of SAR features. Specifically, Fig. 9(a) shows predictions obtained using only the DoS as input features (Set 1); Fig. 9(b) presents estimates derived from the SAR observation model trained with VH backscatter and the DoS (Set 2); and Fig. 9(c) displays results using VH backscatter, coherence, and the DoS as input features. As observed, relying solely on the DoS (Fig. 9(a)) leads to inaccurate estimates. Although the general trend of the true biomass is captured—since the evolution model also provides estimates that are subsequently updated by the Kalman Filter—noticeable errors remain. When VH backscatter is incorporated into the RFR, the accuracy improves overall, except at the beginning of the season (between approximately DoS 0 and DoS 150), where estimation errors remain relatively high. In contrast, when VH intensity

TABLE IX
AVERAGE ACCURACY METRICS OBTAINED WITH THE PROPOSED INTEGRATION ALGORITHM WITH VARYING INPUT FEATURES USED IN THE SAR OBSERVATION MODEL.

Set Number - Input Features	RMSE [kg]	MAE [kg]	Accumulated Biomass Difference [kg·day]
Set 1 - DoS	0.194 (Max.: 0.568)	0.137 (Max.: 0.378)	43.8 (Max.: 175.7)
Set 2 - VH, DoS	0.109 (Max.: 0.265)	0.074 (Max.: 0.143)	16.9 (Max.: 47.2)
Set 3 - VV, DoS	0.115 (Max.: 0.288)	0.108 (Max.: 0.162)	23.3 (Max.: 51.0)
Set 4 - VH, VV, DoS	0.108 (Max.: 0.181)	0.071 (Max.: 0.127)	15.7 (Max.: 31.9)
Set 5 - RVI, DoS	0.108 (Max.: 0.175)	0.070 (Max.: 0.121)	15.7 (Max.: 30.9)
Set 6 - VH coherence, VV coherence, DoS	0.125 (Max.: 0.307)	0.081 (Max.: 0.174)	27.0 (Max.: 56.5)
Set 7 - VH, VH coherence, DoS	0.104 (Max.: 0.164)	0.068 (Max.: 0.114)	14.0 (Max.: 27.3)
Set 8 - VV, VV coherence, DoS	0.105 (Max.: 0.169)	0.069 (Max.: 0.118)	14.1 (Max.: 28.8)
Set 9 - VH, VV, VH coherence, VV coherence, DoS	**0.103 (Max.: 0.155)**	**0.064 (Max.: 0.091)**	**13.8 (Max.: 25.3)**

and coherence are jointly used as input features, the overall accuracy of the biomass estimates increases substantially across the whole season. By comparing Fig. 9(a) and (b), it can be observed that the biomass estimates at the beginning of the season—previously inaccurate when the observation model relied only on VH backscatter and the DoS—become much closer to the ground truth when VH coherence is also included. This improvement was expected during the early growth stages (first 3-4 months), as coherence tends to remain higher when the crops have not yet fully developed. Finally, quantitative metrics of this point are summarized in Table X. As it can be seen, a major improvement is obtained when both VH intensity and coherence are jointly included as input features to the observation model based on the RFR. In fact, accuracy metrics for this point using VH intensity and coherence are very similar to the ones obtained using all available SAR features (see Table IV).

IV. DISCUSSION

In this section, we discuss some benefits of the proposed integration algorithm, compared to alternative methodologies which could have been followed for estimating the biomass of sugarcane crops.

Firstly, as shown in Section III, the methodology offers better accuracy compared to directly applying machine learning, which is currently the most common approach in agricultural remote sensing. Traditional machine learning models use satellite observations as independent samples and ignore temporal information. As a consequency, these methods approaches can lead to inconsistencies and reduced prediction accuracy, particularly when optical imagery is limited, as is the case in the Cauca Valley. The inclusion of SAR data, which can be acquired regardless of the cloud cover, has shown to improve the accuracy of these data-driven models.

Secondly, an alternative approach also based on Artificial Intelligence and that is progressively gaining attraction, consists in the generation of synthetic NDVI images from SAR data [40], [41], [42], [43], [44]. Evidently, this 'conversion' is still an emerging technique and presents several significant challenges. Fundamentally, NDVI and SAR measure different physical properties: NDVI reflects chlorophyll-related canopy greenness, while SAR backscatter responds primarily to canopy structure, surface roughness, and moisture content. This indirect relationship is highly nonlinear and can vary with crop type, phenological stage, soil moisture, and management practices, limiting model generalization across regions or seasons. In the case of sugarcane, some experiments showed that the two types of remote sensing data exhibit different sensitivity [45], which suggests that synthesizing NDVI is not a good approach for this crop type. Further research on this topic is still needed. It is worth noting that in other applications, such as vessel detection [46], artificial intelligence–based methods have demonstrated the potential of converting one type of imagery into the other.

Taking these considerations into account, we consider that dynamical approaches that combine evolution and observation models (in which an initial prediction is subsequently updated using measurements) offer a more robust framework for crop monitoring. While the observation part can be based on machine learning, as demonstrated in this work, a comprehensive framework that fully integrates both evolution and observation processes is essential. In contrast to previous studies [20], [21], [22], [23], which relied on curve-fitting approaches (e.g., n-degree polynomials or double logistic functions) to define the evolution model without explicitly accounting for temporal dynamics, our approach implements two-dimensional transitions to model biomass dynamics, explicitly incorporating temporal information. The inclusion of time in the modelling, as well as the use of transition matrices, was also recently introduced in [47]. However, in that work, a parametrized grid-based filter was used to exploit satellite images for phenology estimation. Such an approach is more complex to define and use than the Kalman filter formulation employed in this work, hence difficulting its adoption in other scenarios.

V. CONCLUSION

In this work we have shown a novel dynamical framework for crop monitoring that integrates time series of both SAR and optical images. This methodology focuses on estimating the biomass of sugarcane crops over an entire growing season.

Results demonstrate that the framework globally achieves highly accurate biomass estimates. The average RMSE and MAE are 0.103 kg (maximum 0.155 kg) and 0.064 kg (maximum 0.091 kg), respectively. These are errors on the order of

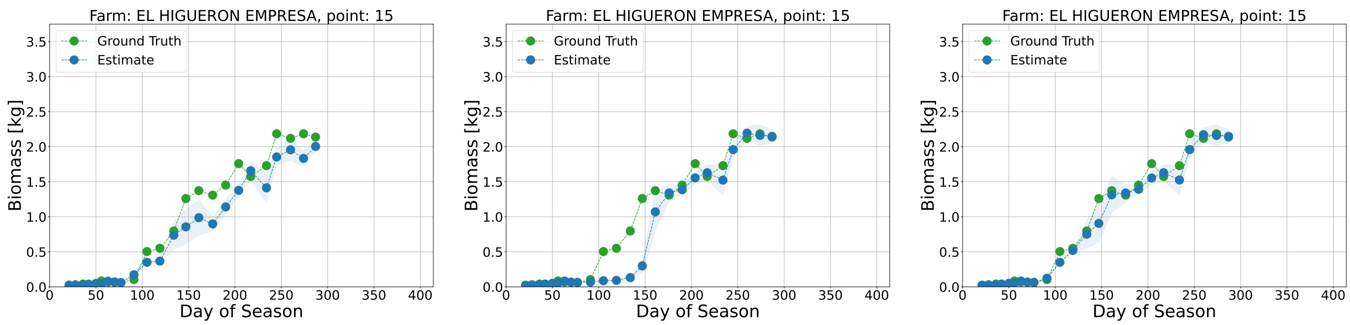

(a) DoS (Set 1). (b) VH, DoS (Set 2) (c) VH, VH coherence, DoS (Set 7)

Fig. 9. Biomass temporal estimation throughout a complete season for point 15 (farm El Higuerón Empresa) using the proposed integration algorithm with different input features used in the SAR observation model.

TABLE X
ACCURACY METRICS OBTAINED WITH THE PROPOSED INTEGRATION ALGORITHM WITH VARYING INPUT FEATURES USED IN THE SAR OBSERVATION MODEL FOR POINT 15.

Set Number - Input Features	RMSE [kg]	MAE [kg]	Accumulated Biomass Difference [kg·day]
Set 1 - DoS	0.322	0.217	69.5
Set 2 - VH, DoS	0.224	0.138	59.2
Set 7 - VH, VH coherence, DoS	0.118	0.068	17.2

one hundred grams for plants producing between 1 and 3 kg of biomass. Also, the error in accumulated biomass difference was, on average after 700 random iterations, 13.8 kg·day (maximum 25.3 kg·day).

The best performance was achieved when all available satellite features were included in the observation models, incorporating dual-polarimetric intensities and coherences from SAR, alongside NDVI from optical imagery. Nevertheless, highly accurate results were also obtained using only single-polarization SAR data (either VV or VH channels) combined with NDVI.

We also compared our methodology against fully data-driven AI-based approaches, which are commonly applied in agricultural remote sensing. As detailed in Section III, these purely AI-based methods underperformed compared to our integrated model. While NDVI theoretically provides better sensitivity to crops than SAR, cloud coverage in the Cauca Valley limited the availability of useful optical images, reducing the accuracy of NDVI-based biomass estimates to levels comparable with SAR-based ones (average RMSE and MAE of 0.212 kg and 0.202 kg, respectively).

We also assessed partial integration using either only SAR or only optical data within our framework. In these scenarios, the proposed method still outperformed AI-based approaches. When using only SAR data, the average RMSE and MAE were 0.13 kg and 0.168 kg, respectively, whereas using only NDVI yielded 0.168 kg and 0.153 kg. Notably, partial integration with NDVI alone performed worse than using only SAR, mainly due to the limited availability of usable optical images, as previously noted.

These results suggest that a dynamical approach is better suited for crop monitoring than purely data-driven methods, particularly in situations where cloud cover reduces the number of available images (NDVI specifically).

A key advantage of this type of dynamical approaches is its inherent flexibility and modularity. Each component of the framework, i.e. the evolution model that produces an initial prediction and the observation model that updates it, can be implemented using a wide range of techniques, including curve-fitting, transition models, or machine learning. Here, we implemented two-dimensional state transitions for the evolution part and ML for the observation models, integrating them by means of the Kalman Filter. This adaptability allows the framework to be eventually tailored to different types of crops, datasets, or monitoring objectives, without altering its overall structure. In our case, we implemented state transitions to address the important variability observed in the biomass which would have caused biased estimates if simpler approaches, such as curve-fitting, had been used. Therefore, the dynamical method can accommodate diverse data sources and modelling strategies, making it highly versatile for agricultural monitoring applications.

In this context, future work will focus on enhancing both the evolution and observation models. The current evolution model, which is entirely based on the measurements collected during the field campaign, will be replaced by a more general crop model for sugarcane. This change is expected to improve generalization and, importantly, reduce the need for extensive ground data collection, which is often unavailable in operational or large-scale applications. Similarly, the current observation models based on machine learning will be replaced with physically based models. While these modifications may not necessarily yield a substantial improvement in prediction accuracy, they are expected to enhance the general applicability of the proposed dynamical framework, enabling its adaptation to different agricultural conditions, geographic regions, and crop types.

Acknowledgments

The authors acknowledge the work of all people involved in the project activities.

This work was funded by the European Union under project DINOSAR - Diagnostic tool that integrates optical, infrared and SAR data, Grant Agreement nr. 101129646.

The work of the UA team was also supported by Grant PID2024-161188OB-C22 funded by MICIU/AEI/10.13039/501100011033 and by ERDF A way of making Europe.

References

[1] S. Fritz, L. See, J. C. L. Bayas, F. Waldner, D. Jacques, I. Becker-Reshef, A. Whitcraft, B. Baruth, R. Bonifacio, J. Crutchfield, F. Rembold, O. Rojas, A. Schucknecht, M. Van der Velde, J. Verdin, B. Wu, N. Yan, L. You, S. Gilliams, S. Mücher, R. Tetrault, I. Moorthy, and I. McCallum, "A comparison of global agricultural monitoring systems and current gaps," *Agricultural Systems*, vol. 168, pp. 258–272, 2019.

[2] A. Sharifi, "Using Sentinel-2 data to predict nitrogen uptake in maize crop," *IEEE Journal of Selected Topics in Applied Earth Observations and Remote Sensing*, vol. 13, pp. 2656–2662, 2020.

[3] A. Moeini Rad, D. Ashourloo, H. Salehi Shahrabi, and H. Nematollahi, "Developing an automatic phenology-based algorithm for rice detection using Sentinel-2 time-series data," *IEEE Journal of Selected Topics in Applied Earth Observations and Remote Sensing*, vol. 12, no. 5, pp. 1471–1481, 2019.

[4] Y. T. Solano-Correa, F. Bovolo, L. Bruzzone, and D. Fernández-Prieto, "A method for the analysis of small crop fields in Sentinel-2 dense time series," *IEEE Transactions on Geoscience and Remote Sensing*, vol. 58, no. 3, pp. 2150–2164, 2020.

[5] H. Pan, Z. Chen, J. Ren, H. Li, and S. Wu, "Modeling winter wheat leaf area index and canopy water content with three different approaches using Sentinel-2 multispectral instrument data," *IEEE Journal of Selected Topics in Applied Earth Observations and Remote Sensing*, vol. 12, no. 2, pp. 482–492, 2019.

[6] A. Kallel, M. D. Mura, S. Fakhfakh, and N. B. Romdhane, "Physics-based fusion of Sentinel-2 and Sentinel-3 for higher resolution vegetation monitoring," *IEEE Transactions on Geoscience and Remote Sensing*, vol. 61, pp. 1–17, 2023.

[7] A. Bégué, D. Arvor, B. Bellon, J. Betbeder, D. De Abelleyra, R. P. D. Ferraz, V. Lebourgeois, C. Lelong, M. Simões, and S. R. Verón, "Remote sensing and cropping practices: A review," *Remote Sensing*, vol. 10, no. 1, 2018.

[8] M. Weiss, F. Jacob, and G. Duveiller, "Remote sensing for agricultural applications: A meta-review," *Remote Sensing of Environment*, vol. 236, p. 111402, 2020.

[9] H. G. Jones and R. A. Vaughan, *Remote sensing of vegetation: principles, techniques and applications*. Oxford, UK: Oxford University Press, 2010.

[10] S. Kandasamy, F. Baret, A. Verger, P. Neveux, and M. Weiss, "A comparison of methods for smoothing and gap filling time series of remote sensing observations – application to MODIS LAI products," *Biogeosciences*, vol. 10, no. 6, pp. 4055–4071, 2013.

[11] J. C. Curlander and R. N. McDonough, *Synthetic aperture radar*. Wiley, New York, 1991, vol. 11.

[12] A. Moreira, P. Prats-Iraola, M. Younis, G. Krieger, I. Hajnsek, and K. P. Papathanassiou, "A tutorial on synthetic aperture radar," *IEEE Geoscience and Remote Sensing Magazine*, vol. 1, no. 1, pp. 6–43, 2013.

[13] H. McNairn and B. Brisco, "The application of C-band polarimetric SAR for agriculture: a review," *Canadian Journal of Remote Sensing*, vol. 30, no. 3, pp. 525–542, 2004.

[14] S. C. Steele-Dunne, H. McNairn, A. Monsivais-Huertero, J. Judge, P.-W. Liu, and K. Papathanassiou, "Radar remote sensing of agricultural canopies: A review," *IEEE Journal of Selected Topics in Applied Earth Observations and Remote Sensing*, vol. 10, no. 5, pp. 2249–2273, 2017.

[15] J. M. Lopez-Sanchez, S. R. Cloude, and J. D. Ballester-Berman, "Rice phenology monitoring by means of SAR polarimetry at X-band," *IEEE Transactions on Geoscience and Remote Sensing*, vol. 50, no. 7, pp. 2695–2709, 2012.

[16] J. M. Lopez-Sanchez, F. Vicente-Guijalba, J. D. Ballester-Berman, and S. R. Cloude, "Polarimetric response of rice fields at C-band: Analysis and phenology retrieval," *IEEE Transactions on Geoscience and Remote Sensing*, vol. 52, no. 5, pp. 2977–2993, 2014.

[17] L. Mascolo, J. M. Lopez-Sanchez, F. Vicente-Guijalba, F. Nunziata, M. Migliaccio, and G. Mazzarella, "A complete procedure for crop phenology estimation with PolSAR data based on the complex Wishart classifier," *IEEE Transactions on Geoscience and Remote Sensing*, vol. 54, no. 11, pp. 6505–6515, 2016.

[18] C. Kuçuk, G. Taskin, and E. Erten, "Paddy-rice phenology classification based on machine-learning methods using multitemporal co-polar X-band SAR images," *IEEE Journal of Selected Topics in Applied Earth Observations and Remote Sensing*, vol. 9, no. 6, pp. 2509–2519, 2016.

[19] H. Yang, B. Pan, N. Li, W. Wang, J. Zhang, and X. Zhang, "A systematic method for spatio-temporal phenology estimation of paddy rice using time series Sentinel-1 images," *Remote Sensing of Environment*, vol. 259, p. 112394, 2021.

[20] F. Vicente-Guijalba, T. Martinez-Marin, and J. M. Lopez-Sanchez, "Crop phenology estimation using a multitemporal model and a Kalman filtering strategy," *IEEE Geoscience and Remote Sensing Letters*, vol. 11, no. 6, pp. 1081–1085, 2014.

[21] ——, "Dynamical approach for real-time monitoring of agricultural crops," *IEEE Transactions on Geoscience and Remote Sensing*, vol. 53, no. 6, pp. 3278–3293, 2015.

[22] C. G. De Bernardis, F. Vicente-Guijalba, T. Martinez-Marin, and J. M. Lopez-Sanchez, "Estimation of key dates and stages in rice crops using dual-polarization SAR time series and a particle filtering approach," *IEEE Journal of Selected Topics in Applied Earth Observations and Remote Sensing*, vol. 8, no. 3, pp. 1008–1018, 2015.

[23] C. De Bernardis, F. Vicente-Guijalba, T. Martinez-Marin, and J. M. Lopez-Sanchez, "Contribution to real-time estimation of crop phenological states in a dynamical framework based on NDVI time series: Data fusion with SAR and temperature," *IEEE Journal of Selected Topics in Applied Earth Observations and Remote Sensing*, vol. 9, no. 8, pp. 3512–3523, 2016.

[24] H. McNairn, X. Jiao, A. Pacheco, A. Sinha, W. Tan, and Y. Li, "Estimating canola phenology using synthetic aperture radar," *Remote Sensing of Environment*, vol. 219, pp. 196–205, 2018.

[25] L. Mascolo, T. Martinez-Marin, and J. M. Lopez-Sanchez, "Optimal grid-based filtering for crop phenology estimation with Sentinel-1 SAR data," *Remote Sensing*, vol. 13, no. 21, 2021.

[26] J. Som-ard, C. Atzberger, E. Izquierdo-Verdiguier, F. Vuolo, and M. Immitzer, "Remote sensing applications in sugarcane cultivation: A review," *Remote Sensing*, vol. 13, no. 20, 2021.

[27] O. Kavats, D. Khramov, K. Sergieieva, and V. Vasyliev, "Monitoring of sugarcane harvest in Brazil based on optical and SAR data," *Remote Sensing*, vol. 12, no. 24, 2020.

[28] R. A. Molijn, L. Iannini, J. Vieira Rocha, and R. F. Hanssen, "Sugarcane productivity mapping through C-band and L-band SAR and optical satellite imagery," *Remote Sensing*, vol. 11, no. 9, 2019.

[29] M. Yeasin, D. Haldar, S. Kumar, R. K. Paul, and S. Ghosh, "Machine learning techniques for phenology assessment of sugarcane using conjunctive SAR and optical data," *Remote Sensing*, vol. 14, no. 14, 2022.

[30] R. E. Kalman *et al.*, "A new approach to linear filtering and prediction problems," *Journal of Basic Engineering*, vol. 82, no. 1, pp. 35–45, 1960.

[31] D. H. Hoekman and J. Reiche, "Multi-model radiometric slope correction of SAR images of complex terrain using a two-stage semi-empirical approach," *Remote Sensing of Environment*, vol. 156, pp. 1–10, 2015.

[32] D. Hoekman, "Speckle ensemble statistics of logarithmically scaled data (radar)," *IEEE Transactions on Geoscience and Remote Sensing*, vol. 29, no. 1, pp. 180–182, 1991.

[33] A. Lopes, R. Touzi, and E. Nezry, "Adaptive speckle filters and scene heterogeneity," *IEEE Transactions on Geoscience and Remote Sensing*, vol. 28, no. 6, pp. 992–1000, 1990.

[34] S. Quegan and J. J. Yu, "Filtering of multichannel SAR images," *IEEE Transactions on Geoscience and Remote Sensing*, vol. 39, no. 11, pp. 2373–2379, 2001.

[35] J. Jones, G. Hoogenboom, C. Porter, K. Boote, W. Batchelor, L. Hunt, P. Wilkens, U. Singh, A. Gijsman, and J. Ritchie, "The DSSAT cropping system model," *European Journal of Agronomy*, vol. 18, no. 3, pp. 235–265, 2003.

[36] S. Hu, L. Shi, K. Huang, Y. Zha, X. Hu, H. Ye, and Q. Yang, "Improvement of sugarcane crop simulation by SWAP-WOFOST model via data assimilation," *Field Crops Research*, vol. 232, pp. 49–61, 2019.

[37] J. R. Norris, *Markov Chains*. Cambridge, UK: Cambridge University Press, 1997.

[38] F. Pedregosa, G. Varoquaux, A. Gramfort, V. Michel, B. Thirion, O. Grisel, M. Blondel, P. Prettenhofer, R. Weiss, V. Dubourg, J. Vanderplas, A. Passos, D. Cournapeau, M. Brucher, M. Perrot, and E. Duchesnay, "Scikit-learn: Machine learning in Python," *Journal of Machine Learning Research*, vol. 12, pp. 2825–2830, 2011.

[39] A. Villarroya-Carpio, J. M. Lopez-Sanchez, and M. E. Engdahl, "Sentinel-1 interferometric coherence as a vegetation index for agriculture," *Remote Sensing of Environment*, vol. 280, October 2022.

[40] T. Roßberg and M. Schmitt, "Estimating NDVI from Sentinel-1 SAR data using deep learning," in *IGARSS 2022 - 2022 IEEE International Geoscience and Remote Sensing Symposium*, 2022, pp. 1412–1415.

[41] P. Soglia, P. Gonzalez, I. Azpiroz, U. Otamendi, M. Quartulli, and S. Salata, "Estimating NDVI from SAR images using conditional generative adversarial networks," in *IGARSS 2023 - 2023 IEEE International Geoscience and Remote Sensing Symposium*, 2023, pp. 5222–5225.

[42] T. Roßberg and M. Schmitt, "Dense NDVI time series by fusion of optical and SAR-derived data," *IEEE Journal of Selected Topics in Applied Earth Observations and Remote Sensing*, vol. 17, pp. 7748–7758, 2024.

[43] Y. Han, J. Huang, F. Ling, X. Gao, W. Cai, and H. Chi, "RDNRnet: A reconstruction solution of NDVI based on SAR and optical images by residual-in-residual dense blocks," *IEEE Transactions on Geoscience and Remote Sensing*, vol. 62, pp. 1–14, 2024.

[44] F.-J. Mesas-Carrascosa, J. T. Arosemena-Jované, S. Cantón-Martínez, F. Pérez-Porras, and J. Torres-Sánchez, "Enhancing crop yield estimation in spinach crops using synthetic aperture radar-derived Normalized Difference Vegetation Index: A Sentinel-1 and Sentinel-2 fusion approach," *Remote Sensing*, vol. 17, no. 8, 2025.

[45] N. den Besten, S. Steele Dunne, A. Mahmud, D. Jackson, B. Aouizerats, R. de Jeu, R. Burger, R. Houborg, M. McGlinchey, and P. van der Zaag, "Understanding Sentinel-1 backscatter response to sugarcane yield variability and waterlogging," *Remote Sensing of Environment*, vol. 290, p. 113555, 2023.

[46] B. Wu, H. Wang, C. Zhang, and J. Chen, "Optical-to-SAR translation based on CDA-GAN for high-quality training sample generation for ship detection in SAR amplitude images," *Remote Sensing*, vol. 16, no. 16, 2024.

[47] L. Mascolo, T. Martinez-Marin, and J. M. Lopez-Sanchez, "A novel dynamical framework for crop phenology estimation with remote sensing," *IEEE Journal of Selected Topics in Applied Earth Observations and Remote Sensing*, vol. 18, pp. 2208–2225, 2025.

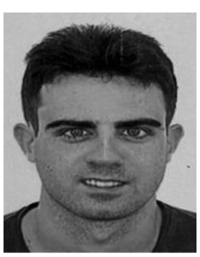

Alejandro Mestre-Quereda (Member IEEE) was born in Madrid, Spain, in 1990. He received the B.S., M.Sc., and Ph.D. degrees in telecommunication engineering from the University of Alicante, Alicante, Spain, in 2015, 2017, and 2019, respectively. From 2019 to 2020, he was a Post-Doctoral Researcher with the Signals, Systems and Telecommunication (SST) Group, University of Alicante. From 2020 to 2024, he worked at Hisdesat Strategic Services, Madrid, as an Earth Observation Applications Engineer, focusing on the development of applications based on the processing of SAR images acquired by the Spanish satellite PAZ, mainly for Defense and Security purposes. In 2024, he returned to the University of Alicante and currently works as a Senior Researcher and Associate Lecturer, carrying out research activities and teaching across several academic programs. His research interests focus on the development of advanced signal processing techniques applied to synthetic aperture radar (SAR) imagery, including SAR interferometry (InSAR), polarimetry (PolSAR), and applied Artificial Intelligence, among others.

Tomas Martinez-Marin (Member, IEEE) received the Tech.Eng. (B.S.) degree in telecommunication engineering from the University of Alcala, Alcala de Henares, Spain, in 1990, and the M.S. and Ph.D. degrees in telecommunications engineering from the Technical University of Madrid, Madrid, Spain, in 1995 and 1999, respectively.

He joined the University of Alcala as an Assistant Professor in 1990. In 1997, he joined the European University of Madrid as an Assistant Professor. Since 2000, he has been with the Department of Physics, System Engineering, and Signal Theory at the University of Alicante, Spain, where he is currently an Associate Professor and the CEO of QuixMind, a spin-off company dedicated to the development and manufacturing of autonomous mobile robots (AMRs). His research interests include reinforcement learning, intelligent vehicles, simultaneous localization and mapping, polarimetric and interferometric techniques, and synthetic aperture radar imaging algorithms.

Juan M. Lopez-Sanchez (Senior Member, IEEE) was born in Alicante, Spain, in 1972. He received the Ingeniero (M.S). and Doctor Ingeniero (Ph.D.) degrees in Telecommunication Engineering from the Technical University of Valencia, Spain, in 1996 and 2000, respectively. From 1998 to 1999 he worked as a predoctoral grantholder at the Space Applications Institute, Joint Research Centre of the European Commission, Ispra, Italy. Since 2000 he leads the Signals, Systems and Telecommunication Group of the University of Alicante, Spain, where he is full professor since November 2011.

His main research interests include microwave remote sensing for inversion of biophysical parameters, polarimetric and interferometric techniques, and applications of radar remote sensing in agriculture and geophysics.

He has coauthored more than 130 papers in refereed journals and more than 170 papers and presentations in international conferences and symposia. In 2001, Dr. Lopez-Sanchez received the Indra Award for the best Ph.D. thesis about radar in Spain. From 2006 to 2012 he was the Chair of the Spanish Chapter of the IEEE Geoscience and Remote Sensing Society.

Carlos Mosquera is an Agricultural Engineer, specialist in Geographic Information Systems (GIS), and MBA, with 28 years of professional experience and more than 20 years of expertise in Precision Agriculture. He has worked as a consultant in the implementation of Precision Agriculture technologies and agronomic management strategies for crops such as sugarcane, rice, oil palm, potarles, coffee, and maize, among others, leading agro-industrial projects for nearly two decades.

Henk Pelgrum received the MS degree in Hydrology and the Ph.D. degree in environmental sciences from the Wageningen University, Wageningen, The Netherlands in 1993 and 2000 respectively. He is currently working for eLEAF, a remote sensing service provider for agricultural water management, based in Amersfoort, the Netherlands. His research interests include mapping of evapotranspiration and biomass growth using optical and thermal infrared remote sensing, image processing and applications of machine learning in remote sensing.

Antonia Skarli received the BSc in Geomatics and Survey Engineering from the Technical Institute of Central Macedonia, Serres, Greece in 2016 and the MSc degree in Geo-Information Science from the Wageningen University, Wageningen, The Netherlands in 2024. She currently works at eLEAF, a remote sensing service provider specializing in agricultural water management based in Amersfoort, the Netherlands. As a Geodata Engineer, she is responsible for data production, delivery, and quality assurance.

Dirk Hoekman received his M.Sc. degree Electrical Engineering from Delft University of Technology, Dept. of Electrical Engineering, The Netherlands in 1981 and his Ph.D. degree Environmental Sciences from Wageningen University, The Netherlands in 1990. He was employed at Wageningen University since 1981 where he held the position of Associate Professor in remote sensing since 1990 until his retirement in 2023. His main interests are the physical aspects of remote sensing, microwave remote sensing and applications of remote sensing in forestry, agriculture, (agro-) hydrology, climate studies and environmental change. He is exploring the scientific use of ALOS PALSAR for tropical peat swamp forest hydrology and forest cover change monitoring in the framework of the JAXA Kyoto & Carbon Initiative. He is also science director at the company SarVision where he focuses on the development and implementation of the SarSentry forest monitoring system based on Sentinel-1 radar.

Corné van der Sande received his MSc degree on Tropical Land Use and as well a MSc degree on Geo-Information Science from the Wageningen University, Wageningen, The Netherlands in 2001. He is working for eLEAF, a remote sensing service provider on biomass growth and agricultural water use. He is a project manager and service developer on making complex earth observation data and algorithm results easily accessible and understandable for non-experts using portals and dashboards. Services delivered are related to compliance monitoring, anomaly detection and variable rate application.